

## Modeling Circumstellar Gas Emission around a White Dwarf Using Cloudy

SIYI XU (许偲艺),<sup>1</sup> SHERRY YEH,<sup>2</sup> LAURA K. ROGERS,<sup>3</sup> AMY STEELE,<sup>4</sup> ERIK DENNIHY,<sup>5</sup> ALEXANDRA E. DOYLE,<sup>6</sup>  
P. DUFOUR,<sup>7</sup> BETH L. KLEIN,<sup>8</sup> CHRISTOPHER J. MANSER,<sup>9,10</sup> CARL MELIS,<sup>11</sup> TINGGUI WANG,<sup>12,13</sup> AND  
ALYCIA J. WEINBERGER<sup>14</sup>

<sup>1</sup>*Gemini Observatory/NSF's NOIRLab, 670 N. A'ohoku Place, Hilo, Hawaii, 96720, USA*

<sup>2</sup>*W. M. Keck Observatory, Waimea, HI, USA*

<sup>3</sup>*Institute of Astronomy, University of Cambridge, Madingley Road, Cambridge CB3 0HA, UK*

<sup>4</sup>*Yerkes Observatory, 373 W. Geneva St., Williams Bay, WI, USA*

<sup>5</sup>*Rubin Observatory Project Office, 950 N. Cherry Ave., Tucson, AZ 85719, USA*

<sup>6</sup>*Earth, Planetary, and Space Sciences, University of California, Los Angeles, Los Angeles, CA 90095, USA*

<sup>7</sup>*Département de Physique, Université de Montréal, C.P. 6128, Succ. Centre-Ville, Montréal, Québec H3C 3J7, Canada*

<sup>8</sup>*Department of Physics and Astronomy, University of California, Los Angeles, CA 90095-1562, USA*

<sup>9</sup>*Astrophysics Group, Department of Physics, Imperial College London, Prince Consort Rd, London, SW7 2AZ, UK*

<sup>10</sup>*Department of Physics, University of Warwick, Coventry CV4 7AL, UK*

<sup>11</sup>*Center for Astrophysics and Space Sciences, University of California, San Diego, CA 92093-0424, USA*

<sup>12</sup>*CAS Key Laboratory for Researches in Galaxies and Cosmology, University of Sciences and Technology of China, Hefei, Anhui 230026, Peoples Republic of China*

<sup>13</sup>*School of Astronomy and Space Sciences, University of Science and Technology of China, Hefei, 230026, Peoples Republic of China*

<sup>14</sup>*Earth and Planets Laboratory, Carnegie Institution for Science, 5241 Broad Branch Rd NW, Washington, DC 20015, USA*

### ABSTRACT

The chemical composition of an extrasolar planet is fundamental to its formation, evolution and habitability. In this study, we explore a new way to measure the chemical composition of the building blocks of extrasolar planets, by measuring the gas composition of the disrupted planetesimals around white dwarf stars. As a first attempt, we used the photo-ionization code CLOUDY to model the circumstellar gas emission around a white dwarf Gaia J0611–6931 under some simplified assumptions. We found most of the emission lines are saturated and the line ratios approaching the ratios of thermal emission; therefore only lower limits to the number density can be derived. Silicon is the best constrained element in the circumstellar gas and we derived a lower limit of  $10^{10.3} \text{ cm}^{-3}$ . In addition, we placed a lower limit on the total amount of gas to be  $1.8 \times 10^{19} \text{ g}$ . Further study is needed to better constrain the parameters of the gas disk and connect it to other white dwarfs with circumstellar gas absorption.

*Keywords:* Circumstellar gas, Chemical abundances, Debris Disks, Planetesimals, Extrasolar Rocky Planets, White Dwarf Stars

### 1. INTRODUCTION

The chemical composition of an exoplanet is an important property, but it is generally hard to constrain because different compositions can have very similar mass-radius relationships (e.g. Dorn et al. 2015). One way to get around this limitation is by observing so called “polluted” white dwarfs, which are actively accreting from disrupted planetesimals. As a result, spectroscopic

observations of the atmospheres of these white dwarfs can be used to measure individual elements, enabling the determination of the chemical compositions of extrasolar planets (e.g. Jura & Young 2014). To zeroth order, the planetary compositions measured from polluted white dwarfs resemble that of bulk Earth: O, Mg, Si, and Fe are the dominant elements in their familiar proportions (e.g. Klein et al. 2011; Xu et al. 2014; Swan et al. 2019; Trierweiler et al. 2023). Objects with a large amount of water and volatile elements have been detected as well (e.g. Xu et al. 2017; Hoskin et al. 2020). However, this kind of analysis is subject to our understanding of

white dwarf physics and many areas are still under active research, e.g. radiative levitation, thermohaline instability, convective overshooting, and 3D effects (Koester et al. 2014; Bauer & Bildsten 2019; Cunningham et al. 2019; Cukanovaite et al. 2021). In addition, the measured abundance ratios can vary by up to an order of magnitude depending on the assumed accretion stage (Koester 2009).

In this study, we explore a new way to constrain the chemical compositions of extrasolar planetesimals by modeling the gas debris around white dwarf stars. There are 21 white dwarfs with a debris disk that has both dust and gas emission (Melis et al. 2020; Dennihy et al. 2020; Gentile Fusillo et al. 2021). Most systems display double-peaked asymmetric emission lines, which are hallmarks of a rotating eccentric disk (Horne & Marsh 1986; Gänsicke et al. 2006; Manser et al. 2021). They are fresh extrasolar planetary material in a transient stage, right after tidal disruption and before being completely accreted onto the white dwarf. The occurrence rate of these gas disks is estimated to be 0.06%, likely because the gaseous components are a rare subset of white dwarf debris disks (Manser et al. 2020). In comparison, the occurrence rate of infrared excess from a debris disk around a white dwarf is about 2–4% (Barber et al. 2016; Wilson et al. 2019). The gas disks can have complex morphologies, as shown by the Doppler tomography observations (e.g. Manser et al. 2016). In addition, the morphology and strength of the emission lines can be variable (Wilson et al. 2014). For some systems, the variability is periodic and it can be explained as a product of precession under the general relativity and gas pressure forces (Miranda & Rafikov 2018; Goksu et al. 2023). In the most extreme case of WD J2100+2122, the emission lines appeared and disappeared within a few months (Dennihy et al. 2020).

Early modeling done by Hartmann et al. (2011, 2016) assumed that the gaseous material is heated by viscous accretion, which overestimates the mass accretion rates and predicts many emission lines that are not observed. The currently favored heating mechanism is photo-ionization, where the central white dwarf is the main energy source (Melis et al. 2010). This concept is demonstrated in the exciting discovery of a sulfur-rich gas disk around a white dwarf, likely from an evaporating giant planet (Gänsicke et al. 2019). The photo-ionization code CLOUDY has also been used to model the circumstellar gas absorption around WD 1124–293 (Steele et al. 2021).

All the rocky gas disk hosts also show infrared excess from a dust disk. The geometrically thin and optically thick dust disk model proposed by Jura (2003) is widely

**Table 1.** Properties of Gaia J0611–6931 from Rogers et al. (2024).

Parameter	Value
Coordinate	06:11:31.70 -69:31:02.15
Gaia ID	5279484614703730944
Spectral Type	DAZ
G (mag)	16.8
Temperature (K)	17749
Surface Gravity ( $\text{cm s}^{-2}$ )	8.14
Mass ( $M_{\odot}$ )	0.702
Radius ( $R_{\odot}$ )	0.0118
Luminosity ( $L_{\odot}$ )	0.012
Distance (pc)	143

used. However, such a model fails to explain bright disks (e.g. Jura et al. 2007) and variable disks (e.g. Xu & Jura 2014; Swan et al. 2020), with the disks that host gaseous emission being among the brightest and most variable (Dennihy et al. 2017; Swan et al. 2020). At least some optically thin dust must be present in the system (Ballering et al. 2022).

The emission line systems provide a new window to study chemical compositions of extrasolar planets. Here, we focus on the gas disk around the white dwarf Gaia J061131.70–693102.15 (referred to as Gaia J0611–6931 for the remainder of the paper). The parameters of the white dwarf are listed in Table 1. Gaia J0611–6931 was first identified as a candidate white dwarf from the Data Release 2 of the *Gaia* mission (Jiménez-Esteban et al. 2018; Gentile Fusillo et al. 2019). Follow-up spectroscopic and photometric observations show that it is indeed a white dwarf with many interesting properties. Gaia J0611–6931 has a strong infrared excess with a fractional luminosity of about 5%, much higher than the typical white dwarf debris disks (Dennihy et al. 2020). It has a heavily polluted atmosphere and photospheric absorption from 10 different elements has been detected (Rogers et al. 2024). In addition, it displays numerous emission lines in the optical and infrared spectra, i.e. O, Na, Mg, Si, and Ca, making it one of the white dwarfs showing the largest variety of gas emission species (Dennihy et al. 2020; Melis et al. 2020; Owens et al. 2023). More importantly, the gas line profiles are symmetric and stable, making Gaia J0611–6931 an ideal target for modeling.

This paper is organized as follows: A summary of the observations and the characteristics of the emission lines around Gaia J0611–6931 is presented in Section 2. The

overall modeling method, including CLOUDY modeling and line profile modeling, is given in Section 3, and its application to Gaia J0611–6931 is in Section 4. Discussion and conclusions are presented in Section 5 and 6, respectively.

## 2. OBSERVATIONS AND DATA ANALYSIS

### 2.1. Observations

Gaia J0611–6931 has been observed extensively using multiple optical, infrared and ultraviolet (UV) spectrographs (Dennihy et al. 2020; Melis et al. 2020; Rogers et al. 2024; Owens et al. 2023). In this paper, we focus on data from the X-SHOOTER on the Very Large Telescope (program IDs: 104.C-0107, 105.202N, and 106.2130), the Cosmic Origins Spectrograph (COS) on the Hubble Space Telescope (Rogers et al. 2024, ID: 16204)<sup>1</sup>, and the Flamings-2 at the Gemini Observatory (GS-2021B-Q-244, Owens et al. 2023). The X-SHOOTER data were obtained on three different dates (i.e., October 15 2019, December 3, 2020, and August 22, 2021 UT), and no significant changes were identified in the shape or the strength of the emission lines. Therefore, all the spectra were combined to have the highest signal to noise ratio (S/N). Stare mode was used for the first two epochs, while nod on slit was used for the last epoch, so the spectra from the NIR arm can be extracted. We used the standard ESO data reduction pipeline esorex (Freudling et al. 2013) and moleculefit (Kausch et al. 2015; Smette et al. 2015). The complete spectrum of Gaia J0611–6931 is shown in Figure 1. The flux calibration is performed using photometry from SkyMapper (Onken et al. 2019). The wavelength is presented in vacuum throughout the paper.

In the infrared beyond 1 micron, the X-SHOOTER data have higher spectral resolution than Flamings-2, which is useful for checking the line identifications presented in Owens et al. (2023). However, the individual exposure time is 300 sec for the NIR arm, which may be too long for proper sky subtraction. That might explain the apparent difference in the line strength between X-SHOOTER and Flamings-2 data.

As an additional check, we obtained a medium resolution ( $R \approx 25,000$ ) optical spectrum of Gaia J0611–6931 with the Magellan Inamori Kyocera Echelle (MIKE) spectrograph (Bernstein et al. 2003) on the 6.5-m Magellan Clay Telescope on August 27, 2021 (UT). The obser-

vation and data reduction were performed using CARPY Kelson et al. (2000); Kelson (2003). The MIKE data provides a wavelength coverage of 3500–5060 Å for the blue arm and 5000–9400 Å for the red arm. The total exposure time is 3111 s and the S/N was 12 at 4000 Å and 14 at 6370 Å. We did not notice any difference between the X-SHOOTER and MIKE spectra.

The spectral classification of Gaia J0611–6931 is DAZ, which means hydrogen lines are the strongest features in the optical spectrum, as can be seen in Figure 1. There are also narrow absorption features from elements heavier than helium in the spectra (giving “Z” in the spectral classification) and the abundance analysis is presented in Rogers et al. (2024). In this paper, we focus on the emission features from the circumstellar gas around Gaia J0611–6931.

### 2.2. Emission Line Analysis

We performed an independent emission line analysis of Gaia J0611–6931 using all available spectra. The identifications for the optical spectra are straightforward because most emission lines are resolved and not blended with other features. There is one triple-peaked feature that extends between 5160 Å to 5190 Å and it has been previously attributed to a blend of Fe II 5170 Å and the Mg I triplet at 5169, 5174 and 5185 Å (Melis et al. 2020; Dennihy et al. 2020). As discussed in Section 4.2, we think this feature is dominated by the Mg I triplet with little contribution from Fe II. The centroid of the Mg I 8809 Å line is shifted by about  $-90 \text{ km s}^{-1}$  compared to all the other emission lines. It is unclear what the cause of this is. There may be a similar wavelength shift for the Mg I 3832 Å line too, though the emission line is a lot weaker, making it difficult to confirm. In the NUV data, there is a broad emission feature around 2800 Å that comes from four Mg I lines (see Figure 2). The infrared line identification in the Flamings-2 data is more challenging because many lines are blended, and our result is consistent with those reported in Owens et al. (2023).

To characterize the emission features, we measured the Full Width at Zero Intensity (FWZI) and the Equivalent Width (EW). For the EW, the uncertainty is dominated by the choice of continuum. For each line, we did several measurements selecting different wavelength regions for estimating the continuum flux. We report the average and the standard deviation of the measurements as the EW and its uncertainty, respectively. We also assume a 3% minimum uncertainty in the EW of the optical lines given the S/N of the spectra. The Si I 3907 Å, Si I 4104 Å, and Ca I 3935 Å lines sit on the slope of the broad hydrogen lines, and therefore have

<sup>1</sup> The HST/COS data presented in this paper were obtained from the Mikulski Archive for Space Telescopes (MAST) at the Space Telescope Science Institute. The specific observations analyzed can be accessed via DOI: 10.17909/zssq-wr33.

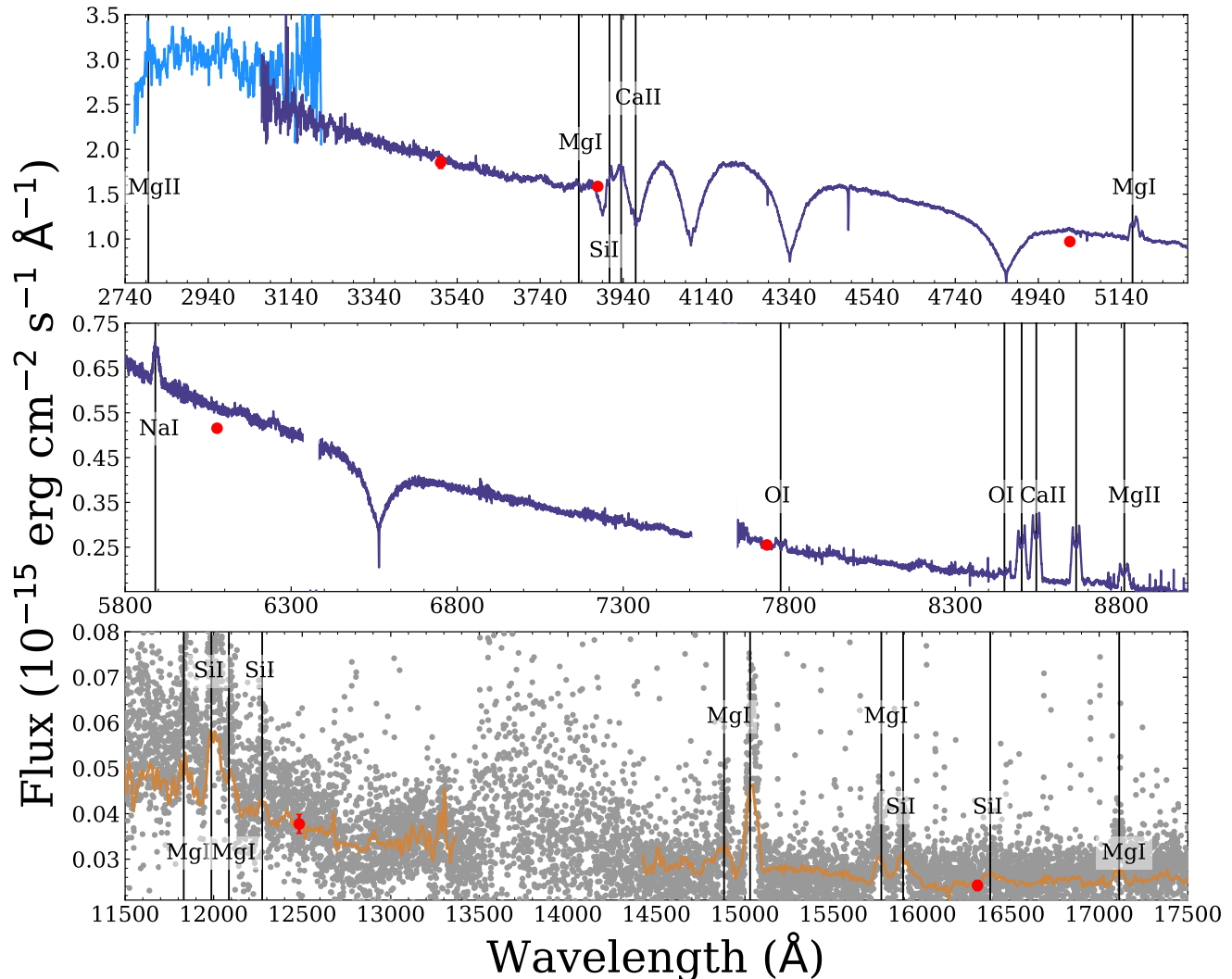


**Figure 1.** The complete spectra of Gaia J0611–6931 with flux calibration anchored to the SkyMapper photometry (red dots). The light blue, dark blue, and orange lines represent data from the HST/COS, the VLT/X-SHOOTER (UVB and VIS arms), and the Gemini/Flamingos-2, respectively. The grey dots are data from the X-SHOOTER NIR arm and are only used for facilitating line identifications. The black lines mark emission features listed in Table 2.

large uncertainties in the EW. The Ca II 3970 Å line is also detected but it is difficult to perform any measurements due to its proximity to He 3971 Å. The EWs and FWZIs of the infrared lines are taken from Owens et al. (2023), which used the Flamingos-2 data. All the measurements are reported in Table 2.

We also measure the integrated line flux of all the emission lines, which is the flux above the continuum in absolute flux units. Note that in some cases, the photospheric absorption is visible in the profile, such as Ca II 3935 Å and O I 8488 Å. However, their overall contribution is small and are therefore not subtracted out in the measurement of line flux. In the case of the Mg II 2796 Å, the contribution from the photospheric

line is significant, as shown in Figure 2. The integrated line flux of the Mg II absorption lines from the model spectrum was added back to derive the flux of the emission feature around Mg II 2796 Å. Similar to the EW measurements, the uncertainty of line flux is dominated by the choice of continuum. For each line, we did several measurements selecting different wavelength ranges given the uncertainties in the FWZIs. We also assume a 3% minimum uncertainty in the line flux for the optical lines and a 10% minimum uncertainty for the infrared lines based on the S/N of the data.

As discussed in Gentile Fusillo et al. (2021), the EW of an emission line is a relative number, which is normalized by the continuum flux. In comparison, the line

**Table 2.** Emission Line Measurements.

Transition (vacuum Å)	FWZI (km s <sup>-1</sup> )	EW (Å)	Line Flux (10 <sup>-16</sup> erg cm <sup>-2</sup> s <sup>-1</sup> )	Other	Reference
O I 7774.1 <sup>†</sup>	1647±351	1.95±0.06	4.8±0.2	O I 7776.3, 7777.5	<i>This Paper</i>
O I 8448.6 <sup>†</sup>	1664±387	2.25±0.07	4.1±0.2	O I 8448.7	<i>This Paper</i>
Na I 5891.6 <sup>†</sup>	1740±479	1.96±0.09	12.3±0.6	Na I 5897.6	<i>This Paper</i>
Mg I 3833.4	1361±63	0.26±0.02	4.1±0.2	...	<i>This Paper</i>
Mg I 5168.8 <sup>†</sup>	2682±633	4.50±0.13	45.2±1.4	Mg I 5174.1, 5185.1	<i>This Paper</i>
Mg I 8809.2	1399±201	6.77±0.20	11.1±0.4	...	<i>This Paper</i>
Mg I 11831*	3226±560	10±2	5.4±0.7	...	Owens et al. (2023)
Mg I 14882 <sup>†</sup>	3558±447	15±2	2.1±0.2	five lines around Mg I 14882	Owens et al. (2023)
Mg I 15029 <sup>†</sup>	2400±122	40±3	13.5±1.4	Mg I 15044, 15052	Owens et al. (2023)
Mg I 17113	1928±363	5.8±1.4	1.9±0.2	...	Owens et al. (2023)
Mg II 2796.4 <sup>†</sup>	3530±600	1.2±0.3	92±10 <sup>‡</sup>	Mg II 2791.6, 2798.8, 2803.5	<i>This Paper</i>
Si I 3906.6	1597±369	1.80±0.14	27.2±2.0	...	<i>This Paper</i>
Si I 4104.1	...	...	...	...	<i>This Paper</i>
Si I 11987 <sup>†</sup>	5800±600	34.6±3.6	15.9±1.6	Si I 11994,12034,12107,Mg I 12086	Owens et al. (2023)
Si I 12274	2165±266	4.9±0.8	1.6±0.2	...	Owens et al. (2023)
Si I & Mg I <sup>†</sup>	5900±600	36±3	9.6±1.0	Si I 15893, 15837, 15964 Mg I 15770,15745,15753	Owens et al. (2023)
Si I 16385 <sup>†</sup>	3697±396	9.2±1.2	1.8±0.2	Si I 16386	Owens et al. (2023)
Ca II 3934.8	1768±381	1.89±0.38	30.6±5.8	...	<i>This Paper</i>
Ca II 3969.6	...	...	...	...	<i>This Paper</i>
Ca II 8500.4	1439±148	13.15±0.40	24.1±0.8	...	<i>This Paper</i>
Ca II 8544.4	1470±207	18.20±0.55	32.8±1.0	...	<i>This Paper</i>
Ca II 8664.5	1530±284	16.70±0.60	28.9±0.9	...	<i>This Paper</i>

<sup>†</sup>This line is a blend and only the strongest transition is listed. The adjacent lines that also contributed to the measurements are listed in the “Other” column.

\* Possibly blended due to the large FWZI.

<sup>‡</sup>From the data, the measured line flux is  $34\pm 8\times 10^{-16}$  erg cm<sup>-2</sup>. However, as shown in Figure 2, there is significant contribution from the photospheric absorption lines. The line flux of the photospheric lines are measured to be  $58\pm 6\times 10^{-16}$  erg cm<sup>-2</sup> from the model. The final number here is the summation of these two values.

flux is an absolute number above the continuum flux, which is a more intrinsic way to characterize the emission line strength. For example, Table 2 shows that the EW of the Ca II 3934 Å line is approximately 10 times weaker than that of the Ca II 8544 Å line. However, that is not due to the relative strength of the emission line, but the difference in the white dwarf continuum flux. As shown in Figure 1, the white dwarf continuum flux is about a factor of 10 higher around Ca II 3934 Å than the Ca infrared triplet region. Therefore, the line strengths for Ca II 3934 Å and Ca II 8544 Å lines are actually similar. For the remainder of the manuscript, we will use line flux as the main observable to compare with the model outputs.

Figure 3 shows a compilation of all the unblended and resolved emission features. The overall shape of the lines is a bit different from element to element, but they all have a similar FWZI of 1530 km s<sup>-1</sup>, half of which corresponds to a Keplerian velocity at a radius of 20R<sub>WD</sub> assuming the gas is in a circular orbit and edge-on. If the disk is inclined relative to our line of sight, the projected velocity would correspond to a smaller radius. The half peak separation is about 350 km s<sup>-1</sup>, which corresponds to a Keplerian velocity at a radius of 70R<sub>WD</sub>. The photospheric component can be seen as the narrow absorption feature around 0 km s<sup>-1</sup> in Ca II 3935 Å and O I doublet at 8448 Å.



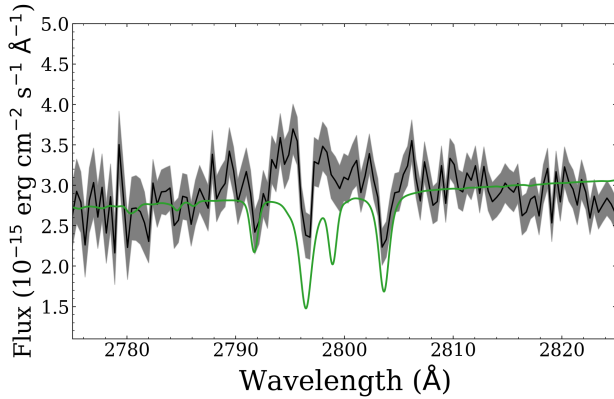


**Figure 2.** A zoomed-in view around the Mg II 2796 Å region. The black line is the data with the grey area indicating the uncertainty. The green line is the best fit atmospheric model, where photospheric absorptions from Mg II are detected (Rogers et al. 2024). There are additional broad Mg II emission lines from the circumstellar gas.

### 3. CIRCUMSTELLAR DISK MODELING

#### 3.1. Cloudy Modeling

Here, we explore modeling the emission lines around Gaia J0611–6931 using the photoionization code CLOUDY (Ferland et al. 2017). The CLOUDY version 17.03 was used for this work. The setup is very similar to those described in Steele et al. (2021). Our configuration uses the cylinder geometry and assumes that the circumstellar gas has a circular orbit, a constant density, and is edge-on. CLOUDY is a 1D code and therefore it only computes the radiative transfer in the radial direction. The central white dwarf is the only ionizing source, whose parameters are listed in Table 1. The main free parameters for the CLOUDY calculation are the radial extent of the disk, the hydrogen number density, and the abundances of different elements, the latter two affecting both the total mass of the gas and the excitation of the different elements.

For CLOUDY outputs, we saved the predicted line intensities for a list of lines, which can be directly compared to the measured line fluxes in Table 2. The line emissivity file, which reports the emergent emissivity as a function of cloud depth, was also saved to calculate the line profile (see Section 3.2). Other output files were also saved following Steele et al. (2021).

#### 3.2. Line Profile Modeling

We adopted an analytical method to compute the line profile, as illustrated in Figure 4. An additional assumption here is that the gas disk is optically thin, therefore we can see the radiation all the way to the inner radius of the disk. As shown in Section 4.2, this assumption is not supported by the CLOUDY calculations. Using po-

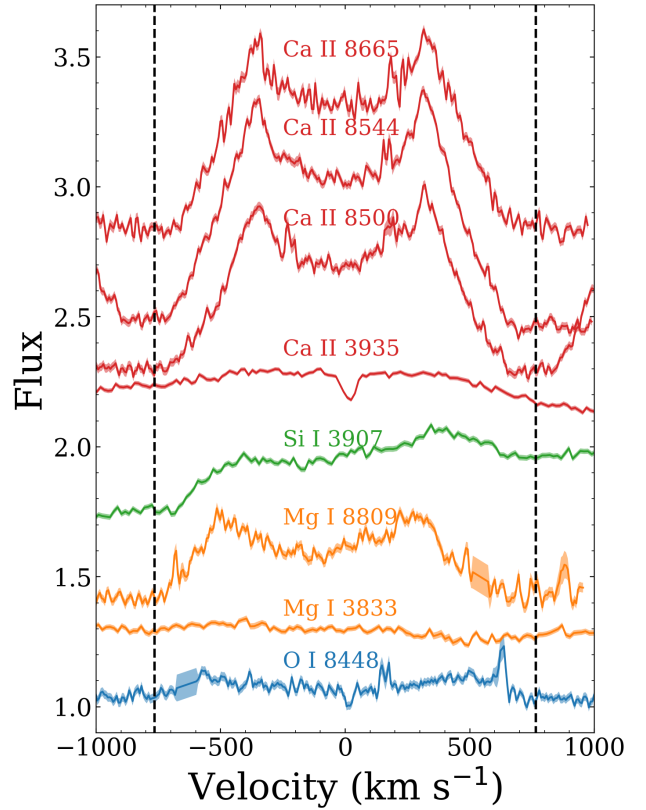


**Figure 3.** A compilation of all the unblended and resolved emission features listed in Table 2. The O I 8448 doublet is also included because their separation is only 0.1 Å. For each emission line, the continuum flux is normalized to one, and then offset for clarity. The velocity is shown in the reference frame of the white dwarf, and therefore the narrow photospheric absorption lines in Ca II 3935 Å and O I 8448 Å appears to be at 0 km s<sup>-1</sup>. The black dashed line marks a FWZI of 1530 km s<sup>-1</sup>, which is the average width of these lines.

lar coordinates, the disk can be approximated as many small patches along the radial and the azimuthal directions. The Keplerian velocity  $V_d$  at a given distance  $d$  from the white dwarf is:

$$V_d = \sqrt{\frac{GM_{\text{wd}}}{d}} = 753 \text{ km s}^{-1} \sqrt{\frac{20R_{\text{wd}}}{d}} \quad (1)$$

where  $G$  is the gravitational constant;  $M_{\text{wd}}$  and  $R_{\text{wd}}$  is the mass and radius of the white dwarf. The velocity along the line of sight  $V_{d,\alpha} = V \times \sin \alpha$ , where  $\alpha$  is the azimuthal angle of the patch.

For each patch, the emissivity is  $\epsilon(d)$ , which is a function of the distance from the white dwarf. The emissivity is also a direct output from CLOUDY. The line profile of the emission line is calculated as the sum of the emissivity of the patch in both the azimuthal and

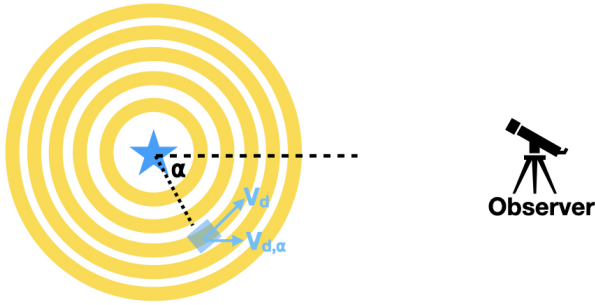


**Figure 4.** A top down view of the geometry of the gas disk. The white dwarf is the blue star and the gas disk is modelled as circular rings. For each small patch in the disk, the line of sight velocity  $V_{d,\alpha}$  can be directly computed and the emissivity can be obtained from CLOUDY.

the radial directions  $\Sigma_{d,\alpha} \epsilon(d)$ , which is a function of the line of sight velocity (or wavelength).

## 4. RESULT

### 4.1. Radial Extent of the Disk

In this section, our goal is to use CLOUDY to better constrain the radial extent of the disk, i.e., the inner disk radius  $R_{in}$  and the outer disk radius  $R_{out}$ . The gas disk is estimated to extend from  $20R_{wd}$  to  $70R_{wd}$  based on the profiles of the double peaked emission lines (see Section 2.2).

The hydrogen number density is another basic input for CLOUDY, but this value is difficult to constrain because hydrogen emission lines are not detected. For the ease of the calculation, we fix the ratio between hydrogen and calcium to be 1 (by number), because it is possible to estimate the density of calcium. Assuming a constant density profile, we can calculate the number density of calcium  $n(\text{Ca})$  as,

$$n(\text{Ca}) = \frac{M_{\text{Ca,gas}}}{u_{\text{Ca}}} \times \frac{1}{\pi(100R_{\text{wd}})^2 \times h} \quad (2)$$

where  $M_{\text{Ca,gas}}$  is the mass of calcium in the circumstellar gas,  $u_{\text{Ca}}$  is the atomic mass of calcium, and  $\pi(100R_{\text{wd}})^2 \times h$  is the estimated volume for the gas, assuming a constant disk scale height  $h$  of  $1 R_{\text{wd}}$ .  $M_{\text{Ca,gas}}$  can be estimated from the mass of Ca in the white dwarf's photosphere  $M_{\text{Ca,phot}}$  ( $7 \times 10^{11}$  g from Rogers et al. 2024), the settling time of Ca in the white dwarf's photosphere  $\tau_{\text{Ca}}$  ( $10^{-2.539}$  yr from Dufour et al. 2016), and the accretion timescale of the disk  $\tau_{\text{diff}}$ ,

$$M_{\text{Ca,gas}} = \frac{M_{\text{Ca,phot}}}{\tau_{\text{Ca}}} \times \tau_{\text{diff}} \quad (3)$$

Using the  $\alpha$  disk model,  $\tau_{\text{diff}}$  can be estimated using Equation (14) of Goksu et al. (2023). Putting in all the numbers, the calcium number density is,

$$n(\text{Ca}) = 4.2 \times 10^7 \text{ cm}^{-3} \times \frac{1R_{\text{wd}}}{h} \times \frac{10^{-2}}{\alpha} \quad (4)$$

The viscosity parameter  $\alpha$  is uncertain by a few orders of magnitude. Therefore, we explore the calcium number density  $n(\text{Ca})$  over a range of values.

We ran a few CLOUDY models using different values of disk scale height and found it is proportional to the absolute strength of the emission lines. A larger scale height means a larger emitting area, and therefore a stronger emission line flux. For this work, the disk scale height is kept at  $1 R_{\text{wd}}$ . Note that  $1 R_{\text{wd}}$  is just a convenient value to adapt; it is larger than the hydrostatic value, which depends on the disk temperature and radius (Goksu et al. 2023).

We compute a grid of CLOUDY calculations with the inner radius  $R_{in}$  of  $15R_{\text{wd}}$ ,  $20R_{\text{wd}}$ ,  $25R_{\text{wd}}$  and the outer radius  $R_{out}$  of  $40R_{\text{wd}}$ ,  $70R_{\text{wd}}$ , and  $100R_{\text{wd}}$ . The result is shown in Figure 5. The separation of the double peak is very sensitive to the outer radius of the disk, but not as much to the inner disk radius. This is a result of the assumed constant density profile of the gas, where most of the disk mass is in the outer part. Therefore, a different density profile will change the radial extent of the disk. The model that best matches the line profile goes from  $20R_{\text{wd}}$  to  $100R_{\text{wd}}$ .

### 4.2. Disk Composition

Here, we attempt to constrain the chemical composition of the circumstellar gas. We focus on the isolated lines listed in Table 2. Mg I 11831 Å is excluded from this analysis, because it is likely to be blended with other lines due to its large FWZI, even though a specific line has not been identified. For Oxygen, there are no isolated lines, so both O I triplet around 7774 Å and the O I doublet at 8488 Å are used. The disk is fixed at 20–100  $R_{\text{wd}}$ , the optimal parameters from Section 4.1.

For each element, we used CLOUDY to compute the curve of growth, which shows the line flux as a function of the number density. In this iteration, we assumed the circumstellar gas has the same abundance as the bulk Earth, and varied the total amount of material. The results are shown in Figure 6. The lines that are mostly likely to be optically thin are the O I 7774 triplet, Mg I 17113 Å, Si I 12274 Å, and Ca II 8500.4 Å. However, given the observed line flux, most of the observed lines are optically thick.

As an additional check, we consider the limiting case where the emission lines are completely saturated and

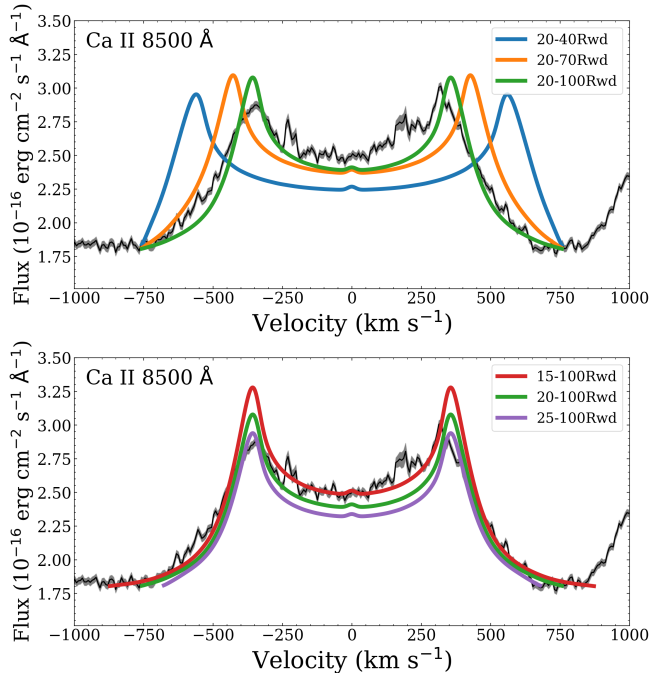


**Figure 5.** A comparison between the observed Ca II 8500 Å line (black line with grey shade representing the uncertainties) and the models with different radial extents of the disk (colored lines). In the top panel, the models were scaled differently to match the overall emission line flux. In the bottom panel, the scaling factors are the same for all the models. Under the assumptions that the gas is optically thin with a constant density, the shape of the line profile is very sensitive to the outer radius of the gas. The model that best matches the observed line profile has a radial extent from  $20R_{WD}$  to  $100R_{WD}$ .

the line flux reaches the Planck blackbody curve with a temperature equal to the gas temperature. In that case, the emission line ratios would equal to blackbody flux ratios. The result for this limiting case is presented in Figure 7. Within the uncertainties, the observed line ratios for O, Mg, and Ca all agree with the blackbody ratios for a temperature between 4,500–10,000 K (the computed gas temperature from CLOUDY, see Section 4.3). For these elements, only an upper limit to the number density can be derived. The only possible exception is Si. The Si I 12274 Å can remain optically thin at a number density of  $10^{9.8} \text{ cm}^{-3}$ , the highest of all the detected emission lines. A silicon density may be derived using this line.

One more iteration of the CLOUDY model was computed to find the abundance that best match the observed line strengths. However, because the number densities of elements are similar, the abundances of one element can affect the line strength of the other element. More tweaks of the abundances are needed to find the best model. Our best fit abundance is listed in Table 3,

**Table 3.** Circumstellar gas abundances from this work and the photospheric abundances from Rogers et al. (2024), with spectroscopic parameters of the white dwarf and abundances from the optical spectra.

Element	Circumstellar ( $\log n(X) \text{ cm}^{-3}$ )	Photosphere ( $\log n(X)/n(H)$ )
O	$> 9.7$	$-3.75 \pm 0.16$
Na	$> 6.8$	-
Mg	$> 9.0$	$-4.61 \pm 0.11$
Si	$> 10.3$	$-4.70 \pm 0.11$
Ca	$> 5.7$	$-6.08 \pm 0.15$

which is able to reproduce the observed line strength within a factor of 2. All the lines have very large optical depths, and therefore only a lower limit can be derived for the density. The hydrogen number density is kept at  $10^{5.7} \text{ cm}^{-3}$ , the same as the number density of calcium. The radial extent of the disk is fixed at  $20\text{--}100R_{WD}$ . As an additional confirmation, different CLOUDY output files are checked to ensure that no other strong lines (such as hydrogen emission or forbidden lines) appear in the model.

As a test to the line fitting code presented in Section 3.2, we computed a line profile for Si I 12274 Å and compared it with data, as shown in Figures 8. The match is respectable, but the spectral resolution of the data is too low to make a proper comparison.

There is a three-peaked feature around 5170 Å, which is a blend of three Mg I lines from 5168.8 Å, 5174.1 Å, 5185.1 Å, and possibly Fe II 5170 Å (Dennihy et al. 2020). Our current model with only Mg already overpredicts the observed feature, and we conclude that the contribution from Fe II 5170 Å in this feature should be minimal.

### 4.3. Disk Temperature

The gas temperature profile from the best fit CLOUDY model is shown in Figure 9. The temperature ranges from 10,000 K around the innermost radius at  $20 R_{WD}$  to 4,500 K to the outer most radius at  $100 R_{WD}$ . The radiation from the white dwarf is the main heat source and cooling is from various emission lines. The gas temperature is similar to the analytical solution proposed by Melis et al. (2010). They described a “Z II” region model, which is akin to an H II region, and the gas is heated by ultraviolet light from the white dwarf and cools by optically thick emission lines. As mentioned in



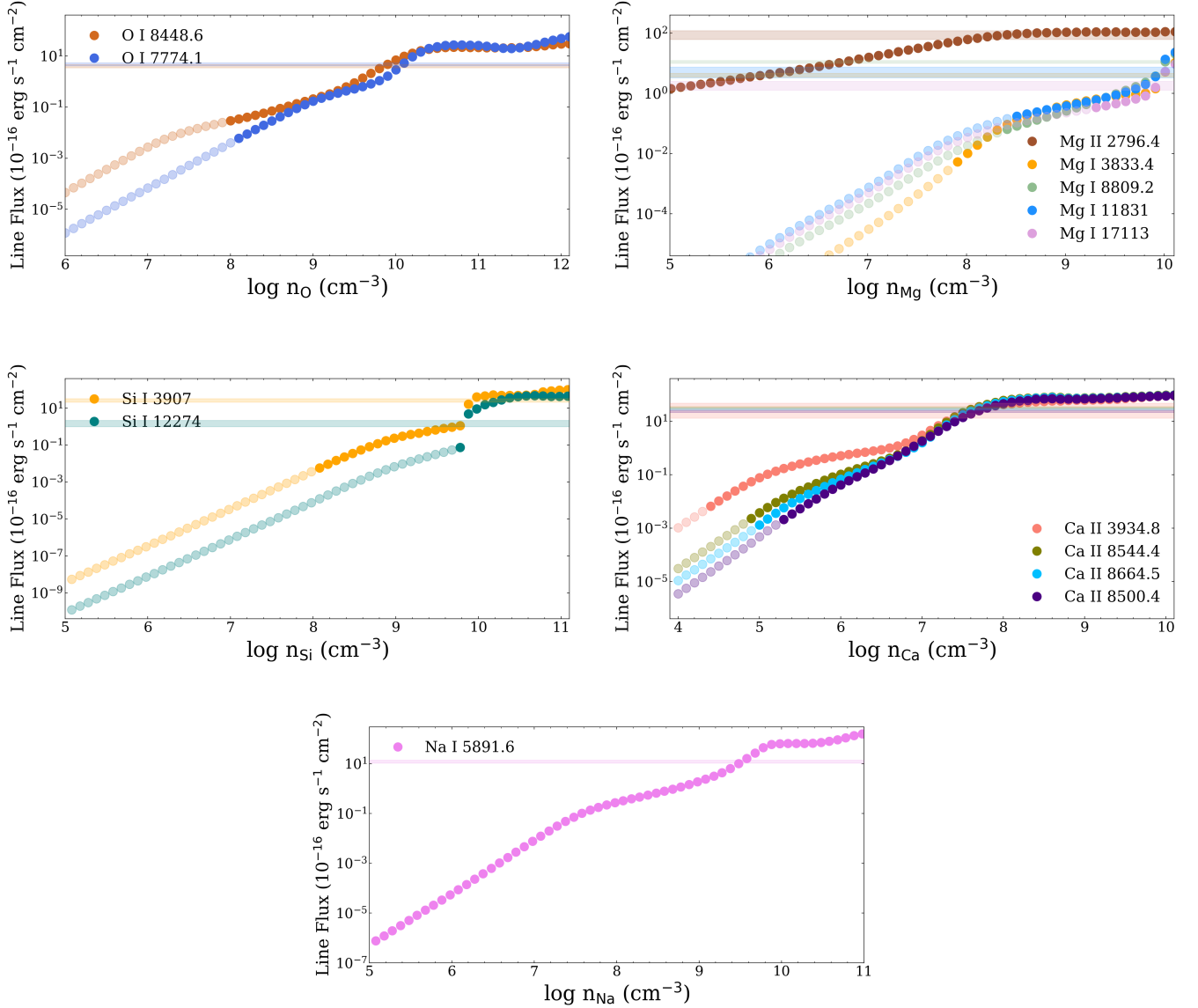


**Figure 6.** CLOUDY models’ prediction of the observed line flux as a function of number density of each element (i.e., the curve of growth). The optically thin regions are marked as transparent circles, while the optically thick regions are marked as solid circles. The optical depth is measured radially. The shaded area represents the  $3\sigma$  range of the observed line flux listed in Table 2. Most of the emission lines appear to be optically thick.

Steele et al. (2021), CLOUDY computes a self-consistent temperature profile, which is an advantage compared to other disk modeling papers assuming an isothermal disk (e.g. Fortin-Archambault et al. 2020; Budaj et al. 2022).

Gaia J0611–6931 has a bright infrared excess with a fractional luminosity of 5% (Dennihy et al. 2020). In fact, a flat disk model failed to reproduce such a strong infrared excess and the disk is either warped or has a significant amount of optically thin dust (Owens et al. 2023). Assuming there is dust around the same region as the circumstellar gas, we compute two dust temperatures using the optically thick model from Jura (2003) and an optically thin model (assuming a blackbody). In

both cases, the dust temperature is much cooler than the gas. It is difficult for the dust and gas to occupy the same region given the large temperature difference. Alternatively, the dust and gas may not occupy the same region, as proposed for the eccentric disk around SDSS J1228+1040 (Goksu et al. 2023). Future work that incorporates both the dust and gas is needed to properly model these systems.

#### 4.4. Other Emission Lines

Rogers et al. (2024) reported detections of photospheric C, S, P, Al, Fe and Ni in Gaia J0611–6931, which were not detected in the circumstellar gas. We

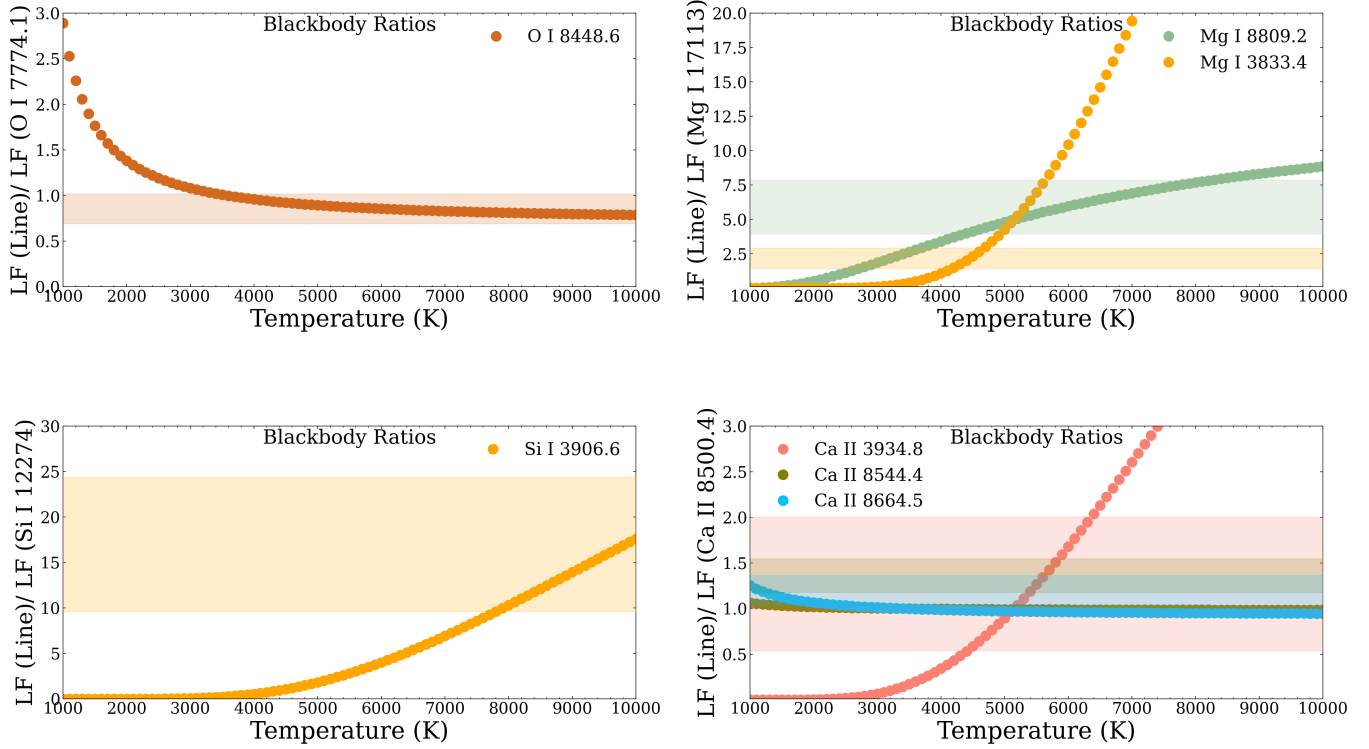


**Figure 7.** The blackbody line ratios as a function of gas temperature. The shaded area represents  $3\sigma$  range of the observed line flux. With the possible exception of Si, all the other line ratios can be explained as the blackbody ratios.

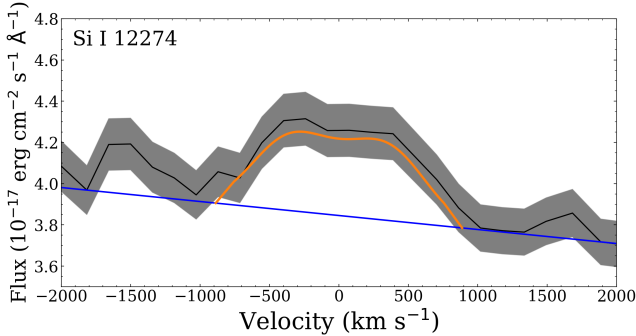


**Figure 8.** A comparison between the observed line profile (black line with grey shaded region indicating  $1\sigma$  uncertainties) and our model prediction (orange line) for Si I 12274 Å.

use the CLOUDY model to make some predictions of the strongest emission lines from these elements, as listed in Table 4. The lines are separated into UV, optical and infrared wavelengths. As discussed in Section 2.2, generally speaking, the UV and optical line fluxes are larger compared to the infrared lines. However, the detectability of the emission lines are better in the infrared, because the white dwarf continuum flux is smaller. Effectively, it means it is possible to detect less luminous lines in the infrared. It will be useful to search for these

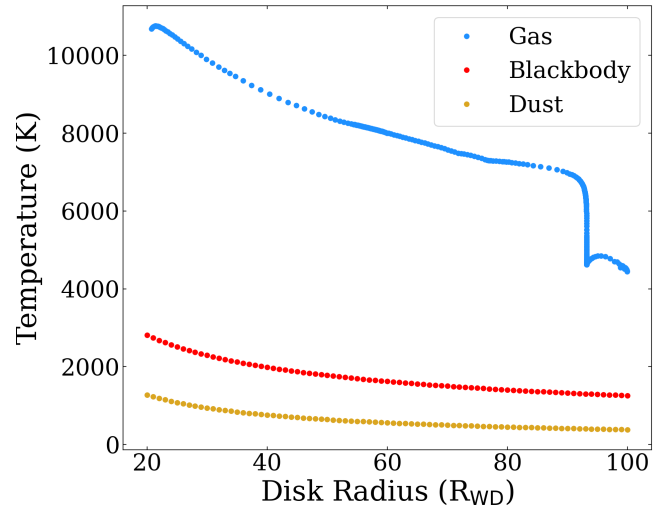


**Figure 9.** Gas temperature as a function of radius from CLOUDY calculations (blue dots). The dust temperature using the model from Jura (2003) (brown dots) and assuming a blackbody (red dots) is also shown for comparison. It is difficult for the dust and gas to co-exist, given the large temperature difference.

additional emission lines to further constrain the composition of the circumstellar gas and compare with the pho-

tospheric abundances. A more extensive study exploring the detectability of the emission lines as a function of white dwarf and disk parameters will be presented in a future work (Steele in prep).

## 5. DISCUSSION

### 5.1. Composition Comparison

We can now compare the abundances of the circumstellar gas around Gaia J0611–6931 with the photospheric abundances. The comparison is shown in Figure 10. The photospheric abundance is taken from Rogers et al. (2024) without any additional correction. The abundance difference between the build-up (the observed abundance in the white dwarf atmosphere equals that of the parent body) and steady state (the observed abundance is the abundance of the parent body modified by differential settling, see details in Dufour et al. 2016) is within 0.2 dex, which does not make a difference in the interpretation here.

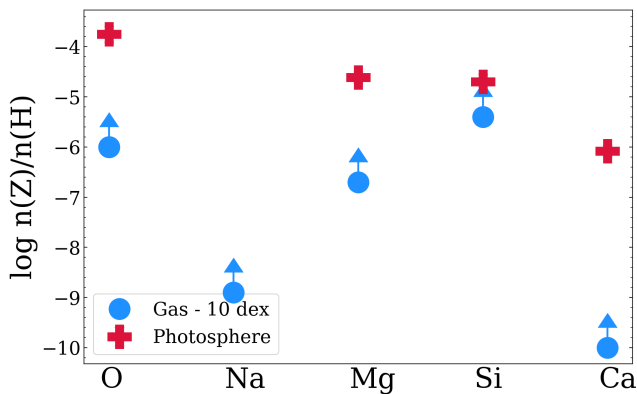


**Figure 10.** Logarithmic number ratios of different heavy elements with respect to hydrogen in the circumstellar gas around Gaia J0611–6931 (blue dots) and the polluted atmosphere of Gaia J0611–6931 (red stars). Relatively speaking, the upper limit to silicon is the most constraining in the circumstellar gas.

Only upper limits were obtained for the elements in the circumstellar gas. Our CLOUDY model assumes that the hydrogen abundance is the same as calcium, because no hydrogen emission line is detected. In Figure 10, we arbitrarily subtracted 10 dex in the number ratios for circumstellar gas, to put the compositions of the photosphere and the gas in a similar scale. For Gaia J0611–6931, we found the upper limit to Si is the most constraining in the gas.

### 5.2. Mass of the Gas Disk

The mass of the gas disk can be estimated using the number densities in Table 3. The other assumption

is that the disk extends from 20 to 100  $R_{\text{wd}}$  with a constant scale height of 1  $R_{\text{wd}}$ . We can derive a lower limit on the mass of the gas disk mass to be  $1.8 \times 10^{19}$  g, considering O, Si, Ca, Na and Mg. On the other hand, the total amount of heavy elements in the atmosphere of Gaia J0611–6931 is  $7.1 \times 10^{16}$ , which is much smaller than the minimum mass of the gas disk. Taking the mass accretion rate of  $6.57 \times 10^8$  g  $\text{s}^{-1}$  (Rogers et al. 2024), the minimum gas disk life time is 900 yr.

Our derived minimum gas disk mass of  $1.8 \times 10^{19}$  g is close to the gas mass estimate of  $10^{21}$  g for another white dwarf SDSS J1228+1040 using emission line kinematics (Goksu et al. 2023). In other studies to model the circumstellar gas absorption around white dwarfs, the estimated gas mass is about  $10^{16}$  g for WD 1145+017 (Fortin-Archambault et al. 2020) and  $5 \times 10^8 - 1.3 \times 10^{16}$  g for WD 1124–293 (Steele et al. 2021). Compared to emission line detection, circumstellar absorption lines appear to be much more sensitive to small amount of circumstellar material around white dwarfs.

### 5.3. Future Improvements

In this paper, we developed a simple model for the circumstellar gas around the white dwarf Gaia J0611–6931 using CLOUDY. The number densities of O, Si, Ca, Na and Mg are constrained and a minimum gas disk mass is also derived. Here, we discuss the limitations of the current work and future improvements.

**Modeling: disk geometry & density profile & scale height.** Our CLOUDY model takes the simplest assumption that the gas disk is edge-on with a constant density profile and a constant scale height. This is a major uncertainty that affects the projected velocities, radiative transfer, disk temperature, and line flux. In addition, radiative transfer is only computed along the radial direction, and not in the vertical direction. Given the large optical depth in the radial direction, the line photons may escape from the disk surface. Future work is needed to explore these possibilities.

**Observation: emission lines with resolved profiles.** This study demonstrates the advantage of using infrared emission lines, which are more likely to be optically thin and therefore are better probes of the density of the gas. However, due to the lower spectral resolution of the infrared data, the line profiles are not resolved and most of the infrared lines are heavily blended, limiting its usage. Future observations with a higher spectral resolution that resolves the profiles of the infrared emission lines will be particularly useful in constraining the parameters of the disk and the abundances. It will also be useful to search for additional emissions from other

**Table 4.** CLOUDY Predicted Strong Emission Lines from Other Elements for Gaia J0611–6931

Ions	Transition (vacuum Å)		
	UV (1000-3000 Å)	Optical (3000-10,000 Å)	Infrared (10,000-100,000 Å)
C I	1561.5, 1656.2, 1658.1	4622.8, 8729.4, 9852.9	10710, 10757, 14547
C II	1334.5, 1335.6, 1335.7	4746.1, 6584.8, 7233.3	...
S I	1807.3, 1820.3, 1826.2	7727.1, 9230.7, 9240.2	10458, 10824, 11309
S II	1102.4, 1250.6, 1253.8	4069.7, 4077.6, 6732.6	10290, 10323, 10339
P I	1775.0, 1787.6, 2136.9	5334.0, 5341.1, 8789.9	13538, 13566, 13584
P II	1152.8, 1157.0, 1159.0	4670.5, 4737.9, 7878.2	11471, 11886, 11258
Al I	1775.7, 2071.5, 2398.0	3083.0, 3093.6, 3962.6	13127, 13155, 16755
Al II	1670.8, 1725.0, 1763.9	3901.8, 7065.6	10126
Fe I	2181.0, 2485.0, 2527.3	3441.6, 3721.0, 3738.2	11611, 11887, 11976
Fe II	2396.3, 2612.7, 2626.5	3256.9, 3278.3, 5019.8	12570, 13558, 14335
Ni I	1623.7	3036.6, 3311.9, 3481.1	31199, 58933, 75066
Ni II	1324.1, 1375.7, 1744.2	3439.9, 3627.9, 7379.9	10462, 19393, 66360

elements (such as those listed in Table 4) that are currently not detected.

## 6. CONCLUSIONS

In this paper, we present a model using the photoionization code CLOUDY and an analytical method to study the circumstellar gas around the white dwarf Gaia J0611–6931. Emission lines from five different species – O, Na, Mg, Si and Ca – are detected around Gaia J0611–6931. This detection is based on a comprehensive dataset that spans the ultraviolet, optical and infrared spectra. The emission lines are symmetric and stable, displaying no significant changes over a three year period and making it an ideal system for modeling.

We provide here a first estimate for the composition of a refractory gaseous debris disk. Here is a summary of the main conclusions.

- The line flux for each emission line is measured and compared with the CLOUDY output to constrain the abundances. For future work, we would like to encourage the use of the line flux (in favor of equivalent width), which is a more absolute way to characterize the emission line strength and allows disks to be directly compared to one another.

- Our model takes some simple assumptions: (i) the gas is on a circular orbit, (ii) the disk is edge-on and radiative transfer is only computed along the radial direction, (iii) a constant density profile, (iv) a constant disk scale height. Based on these assumptions, we find the best fit model requires the gas to extend from  $20R_{\text{wd}}$  to  $100R_{\text{wd}}$ . The disk would be closer to the white dwarf if it is more inclined.

- We found most of the emission lines are completely saturated, and the line ratios approach the blackbody ratios. Only a lower limit to the number density can be derived. One complication is that the strength of a line from an element X depends on both the abundance of that particular element X and the other elements. Relatively speaking, silicon can be best constrained in the circumstellar gas with a lower limit of  $10^{10.3} \text{ cm}^{-3}$ .

- The gas temperature is estimated to be 10,000 K to 4,500 K. Likely, the circumstellar gas is much closer to the white dwarf than the circumstellar dust disk. We also placed a lower limit on the mass of the gas to be  $1.8 \times 10^{19} \text{ g}$ .

- Several improvements are needed in order to apply this method to a broader sample of white dwarfs with circumstellar gas. Modeling the composition of circumstellar gas may represent a novel approach to constraining the composition of extrasolar planetesimals.

*Acknowledgements.* We would like to thank the referee Y. Wu, whose comments significantly improved the quality of the manuscript. We would like to thank F. Lagos, O. Toloza, and B. Gänsicke on discussing the usage of CLOUDY. We thank N. Jiang and B. Zuckerman for discussing the content of the paper.

This research is based on observations made with the NASA/ESA Hubble Space Telescope obtained from the Space Telescope Science Institute, which is operated by the Association of Universities for Research in Astronomy, Inc., under NASA contract NAS 526555. These observations are associated with program 16204.

S. Xu is supported by the international Gemini Observatory, a program of NSF's NOIRLab, which is managed by the Association of Universities for Research in Astronomy (AURA) under a cooperative agreement with the National Science Foundation on behalf of the Gemini partnership of Argentina, Brazil, Canada, Chile, the Republic of Korea, and the United States of America. S. Blouin is a Banting Postdoctoral Fellow and a CITA National Fellow, supported by the Natural Sciences and Engineering Research Council of Canada (NSERC). L. Rogers acknowledges support of a Royal Society University Research Fellowship,

URF\R1\211421 and an ESA Co-Sponsored Research Agreement No. 4000138341/22/NL/GLC/my = Tracing the Geology of Exoplanets.

This research was supported in part by the National Science Foundation under Grant No. NSF PHY-1748958.

*Software:* Astropy (Astropy Collaboration et al. 2013; Price-Whelan et al. 2018; Astropy Collaboration et al. 2022), Cloudy (Ferland et al. 2017), Matplotlib (Hunter 2007)

## REFERENCES

- Astropy Collaboration, Robitaille, T. P., Tollerud, E. J., et al. 2013, *A&A*, 558, A33, doi: [10.1051/0004-6361/201322068](https://doi.org/10.1051/0004-6361/201322068)
- Astropy Collaboration, Price-Whelan, A. M., Lim, P. L., et al. 2022, *ApJ*, 935, 167, doi: [10.3847/1538-4357/ac7c74](https://doi.org/10.3847/1538-4357/ac7c74)
- Ballering, N. P., Levens, C. I., Su, K. Y. L., & Cleeves, L. I. 2022, *ApJ*, 939, 108, doi: [10.3847/1538-4357/ac9a4a](https://doi.org/10.3847/1538-4357/ac9a4a)
- Barber, S. D., Belardi, C., Kilic, M., & Gianninas, A. 2016, *MNRAS*, 459, 1415, doi: [10.1093/mnras/stw683](https://doi.org/10.1093/mnras/stw683)
- Bauer, E. B., & Bildsten, L. 2019, *ApJ*, 872, 96, doi: [10.3847/1538-4357/ab0028](https://doi.org/10.3847/1538-4357/ab0028)
- Bernstein, R., Shectman, S. A., Gunnels, S. M., Mochnicki, S., & Athey, A. E. 2003, in *Society of Photo-Optical Instrumentation Engineers (SPIE) Conference Series*, Vol. 4841, *Instrument Design and Performance for Optical/Infrared Ground-based Telescopes*, ed. M. Iye & A. F. M. Moorwood, 1694–1704, doi: [10.1117/12.461502](https://doi.org/10.1117/12.461502)
- Budaj, J., Maliuk, A., & Hubeny, I. 2022, *A&A*, 660, A72, doi: [10.1051/0004-6361/202141924](https://doi.org/10.1051/0004-6361/202141924)
- Cukanovaite, E., Tremblay, P.-E., Bergeron, P., et al. 2021, *MNRAS*, 501, 5274, doi: [10.1093/mnras/staa3684](https://doi.org/10.1093/mnras/staa3684)
- Cunningham, T., Tremblay, P.-E., Freytag, B., Ludwig, H.-G., & Koester, D. 2019, *MNRAS*, 488, 2503, doi: [10.1093/mnras/stz1759](https://doi.org/10.1093/mnras/stz1759)
- Dennihy, E., Clemens, J. C., Debes, J. H., et al. 2017, *ApJ*, 849, 77, doi: [10.3847/1538-4357/aa8ef2](https://doi.org/10.3847/1538-4357/aa8ef2)
- Dennihy, E., Xu, S., Lai, S., et al. 2020, *ApJ*, 905, 5, doi: [10.3847/1538-4357/abc339](https://doi.org/10.3847/1538-4357/abc339)
- Dorn, C., Khan, A., & Heng, K., et al. 2015, *A&A*, 577, A83, doi: [10.1051/0004-6361/201424915](https://doi.org/10.1051/0004-6361/201424915)
- Dufour, P., Blouin, S., & Coutu, S., et al. 2016, *ASPC*, in press, *ArXiv: 1610.00986*
- Ferland, G. J., Chatzikos, M., Guzmán, F., et al. 2017, *RMxAA*, 53, 385, doi: [10.48550/arXiv.1705.10877](https://doi.org/10.48550/arXiv.1705.10877)
- Fortin-Archambault, M., Dufour, P., & Xu, S. 2020, *ApJ*, 888, 47, doi: [10.3847/1538-4357/ab585a](https://doi.org/10.3847/1538-4357/ab585a)
- Freudling, W., Romaniello, M., Bramich, D. M., et al. 2013, *A&A*, 559, A96, doi: [10.1051/0004-6361/201322494](https://doi.org/10.1051/0004-6361/201322494)
- Gänsicke, B. T., Marsh, T. R., Southworth, J., & Rebassa-Mansergas, A. 2006, *Science*, 314, 1908, doi: [10.1126/science.1135033](https://doi.org/10.1126/science.1135033)
- Gänsicke, B. T., Schreiber, M. R., Toloza, O., et al. 2019, *Nature*, 576, 61, doi: [10.1038/s41586-019-1789-8](https://doi.org/10.1038/s41586-019-1789-8)
- Gentile Fusillo, N. P., Tremblay, P.-E., Gänsicke, B. T., et al. 2019, *MNRAS*, 482, 4570, doi: [10.1093/mnras/sty3016](https://doi.org/10.1093/mnras/sty3016)
- Gentile Fusillo, N. P., Manser, C. J., Gänsicke, B. T., et al. 2021, *MNRAS*, 504, 2707, doi: [10.1093/mnras/stab992](https://doi.org/10.1093/mnras/stab992)
- Goksu, A., Kutra, T., & Wu, Y. 2023, *arXiv e-prints*, *arXiv:2308.01234*, doi: [10.48550/arXiv.2308.01234](https://doi.org/10.48550/arXiv.2308.01234)
- Hartmann, S., Nagel, T., Rauch, T., & Werner, K. 2011, *A&A*, 530, A7, doi: [10.1051/0004-6361/201116625](https://doi.org/10.1051/0004-6361/201116625)
- . 2016, *A&A*, 593, A67, doi: [10.1051/0004-6361/201628403](https://doi.org/10.1051/0004-6361/201628403)
- Horne, K., & Marsh, T. R. 1986, *MNRAS*, 218, 761, doi: [10.1093/mnras/218.4.761](https://doi.org/10.1093/mnras/218.4.761)
- Hoskin, M. J., Toloza, O., Gänsicke, B. T., et al. 2020, *MNRAS*, 499, 171, doi: [10.1093/mnras/staa2717](https://doi.org/10.1093/mnras/staa2717)
- Hunter, J. D. 2007, *Computing in Science Engineering*, 9, 90, doi: [10.1109/MCSE.2007.55](https://doi.org/10.1109/MCSE.2007.55)
- Jiménez-Esteban, F. M., Torres, S., Rebassa-Mansergas, A., et al. 2018, *MNRAS*, 480, 4505, doi: [10.1093/mnras/sty2120](https://doi.org/10.1093/mnras/sty2120)
- Jura, M. 2003, *ApJL*, 584, L91, doi: [10.1086/374036](https://doi.org/10.1086/374036)
- Jura, M., Farihi, J., & Zuckerman, B. 2007, *ApJ*, 663, 1285, doi: [10.1086/518767](https://doi.org/10.1086/518767)
- Jura, M., & Young, E. D. 2014, *Annual Review of Earth and Planetary Sciences*, 42, 45, doi: [10.1146/annurev-earth-060313-054740](https://doi.org/10.1146/annurev-earth-060313-054740)
- Kausch, W., Noll, S., Smette, A., et al. 2015, *A&A*, 576, A78, doi: [10.1051/0004-6361/201423909](https://doi.org/10.1051/0004-6361/201423909)
- Kelson, D. D. 2003, *PASP*, 115, 688, doi: [10.1086/375502](https://doi.org/10.1086/375502)



- Kelson, D. D., Illingworth, G. D., van Dokkum, P. G., & Franx, M. 2000, *ApJ*, 531, 159, doi: [10.1086/308445](https://doi.org/10.1086/308445)
- Klein, B., Jura, M., Koester, D., & Zuckerman, B. 2011, *ApJ*, 741, 64, doi: [10.1088/0004-637X/741/1/64](https://doi.org/10.1088/0004-637X/741/1/64)
- Koester, D. 2009, *A&A*, 498, 517, doi: [10.1051/0004-6361/200811468](https://doi.org/10.1051/0004-6361/200811468)
- Koester, D., Gänsicke, B. T., & Farihi, J. 2014, *A&A*, 566, A34, doi: [10.1051/0004-6361/201423691](https://doi.org/10.1051/0004-6361/201423691)
- Manser, C. J., Gänsicke, B. T., Gentile Fusillo, N. P., et al. 2020, *MNRAS*, 493, 2127, doi: [10.1093/mnras/staa359](https://doi.org/10.1093/mnras/staa359)
- Manser, C. J., Gänsicke, B. T., Marsh, T. R., et al. 2016, *MNRAS*, 455, 4467, doi: [10.1093/mnras/stv2603](https://doi.org/10.1093/mnras/stv2603)
- Manser, C. J., Dennihy, E., Gänsicke, B. T., et al. 2021, *MNRAS*, 508, 5657, doi: [10.1093/mnras/stab2948](https://doi.org/10.1093/mnras/stab2948)
- Melis, C., Jura, M., Albert, L., Klein, B., & Zuckerman, B. 2010, *ApJ*, 722, 1078, doi: [10.1088/0004-637X/722/2/1078](https://doi.org/10.1088/0004-637X/722/2/1078)
- Melis, C., Klein, B., Doyle, A. E., et al. 2020, *ApJ*, 905, 56, doi: [10.3847/1538-4357/abbdfa](https://doi.org/10.3847/1538-4357/abbdfa)
- Miranda, R., & Rafikov, R. R. 2018, *ApJ*, 857, 135, doi: [10.3847/1538-4357/aab9a2](https://doi.org/10.3847/1538-4357/aab9a2)
- Onken, C. A., Wolf, C., Bessell, M. S., et al. 2019, *PASA*, 36, e033, doi: [10.1017/pasa.2019.27](https://doi.org/10.1017/pasa.2019.27)
- Owens, D., Xu, S., Manjavacas, E., et al. 2023, *AJ*, 166, 5, doi: [10.3847/1538-3881/accc25](https://doi.org/10.3847/1538-3881/accc25)
- Price-Whelan, A. M., Sipőcz, B. M., Günther, H. M., et al. 2018, *AJ*, 156, 123, doi: [10.3847/1538-3881/aabc4f](https://doi.org/10.3847/1538-3881/aabc4f)
- Rogers, L. K., Bonsor, A., Xu, S., et al. 2024, *MNRAS*, 527, 6038, doi: [10.1093/mnras/stad3557](https://doi.org/10.1093/mnras/stad3557)
- Smette, A., Sana, H., Noll, S., et al. 2015, *A&A*, 576, A77, doi: [10.1051/0004-6361/201423932](https://doi.org/10.1051/0004-6361/201423932)
- Steele, A., Debes, J., Xu, S., Yeh, S., & Dufour, P. 2021, *ApJ*, 911, 25, doi: [10.3847/1538-4357/abc262](https://doi.org/10.3847/1538-4357/abc262)
- Swan, A., Farihi, J., Koester, D., et al. 2019, *MNRAS*, 490, 202, doi: [10.1093/mnras/stz2337](https://doi.org/10.1093/mnras/stz2337)
- Swan, A., Farihi, J., Wilson, T. G., & Parsons, S. G. 2020, *MNRAS*, 496, 5233, doi: [10.1093/mnras/staa1688](https://doi.org/10.1093/mnras/staa1688)
- Trierweiler, I. L., Doyle, A. E., & Young, E. D. 2023, *PSJ*, 4, 136, doi: [10.3847/PSJ/acdef3](https://doi.org/10.3847/PSJ/acdef3)
- Wilson, D. J., Gänsicke, B. T., Koester, D., et al. 2014, *MNRAS*, 445, 1878, doi: [10.1093/mnras/stu1876](https://doi.org/10.1093/mnras/stu1876)
- Wilson, T. G., Farihi, J., Gänsicke, B. T., & Swan, A. 2019, *MNRAS*, 1000, doi: [10.1093/mnras/stz1050](https://doi.org/10.1093/mnras/stz1050)
- Xu, S., & Jura, M. 2014, *ApJL*, 792, L39, doi: [10.1088/2041-8205/792/2/L39](https://doi.org/10.1088/2041-8205/792/2/L39)
- Xu, S., Jura, M., Koester, D., Klein, B., & Zuckerman, B. 2014, *ApJ*, 783, 79, doi: [10.1088/0004-637X/783/2/79](https://doi.org/10.1088/0004-637X/783/2/79)
- Xu, S., Zuckerman, B., Dufour, P., et al. 2017, *ApJL*, 836, L7, doi: [10.3847/2041-8213/836/1/L7](https://doi.org/10.3847/2041-8213/836/1/L7)